Resonant Holographic Detection of Hydroxyl Radicals in Reacting Flows

J. E. Craig* and M. Azzazy†
Spectron Development Laboratory, Costa Mesa, California
and
C. C. Poon‡
IBM Corporation, San Jose, California

Holographic wavefront diagnostics are particularly well-suited for spectroscopic applications where at least two measurements are generally required to determine temperature and concentration. Holographic wavefront reconstruction allows both refraction and absorption measurements by interferometric phase and intensity detection, respectively. For resonant wavelengths, the refractivity and absorptivity are uniquely related to temperature and concentration of the resonant species by the linear dispersion relations. The theoretical basis for the technique is examined for the hydroxyl radical appearing in methane-air flames. One-dimensional, methane-air flame experiments are described in which the holographic technique is shown to be viable at ultraviolet wavelengths. The technique is shown, in theory, to have excellent sensitivity to density and temperature.

Introduction

THE design of advanced combustion systems with emphasis on increased conversion efficiency and pollution control requires detailed knowledge of the complex physical and chemical processes occurring simultaneously within the reaction zone. The measurement of basic parameters such as temperature, species concentration, and flow velocity is essential to reaching an understanding of the mechanisms that control the relevant reaction phenomena.

Practical combustion system flows are highly turbulent (sometimes unsteady) with highly variable length scales with potentially submillisecond event times. A useful measurement, therefore, must entail observations obtained within the period of such a time scale. With the availability of high-intensity, high-precision pulsed tunable lasers, advances in diagnostic measurements are making important contributions to an increased level of understanding, albeit using simple flow configurations and fuels of simple structure having "tractable" chemistry. Several important diagnostic techniques have become available within the last decade[1] and have demonstrated successes in quantifying gas temperatures and species concentrations. The techniques used most often are: laser absorption,[2] laser-induced fluorescence,[3-5] Rayleigh scattering,[6] spontaneous Raman scattering,[7] and coherent anti-Stokes Raman scattering.[8]

The relatively new multiple-point diagnostic techniques for species concentration measurement are being actively pursued at several institutions—Sandia, Stanford, and the National Bureau of Standards (NBS).[4,5,9,10] The experimental work at Sandia and Stanford utilizes laser-induced fluorescence observed from thin sheets of laser light directed through an absorbing gas; while the work at NBS has investigated the theoretical basis for multiple-wavelength, multiple-angle, laser tomography. A recent application of this approach in combustion has been in the concentration measurements of an axisymmetric nonreactive methane jet using multiangular absorption.[11] The jet was isothermal so that measured absorptivity was relatable to concentration. The latest work at NBS seeks to extend this technique to the nonisothermal case, as is the case in a combustor.[9,10] In this respect, the combined effect of temperature and concentration in absorption is inseparable without additional diagnostics or theoretical modeling. To this end, existing diagnostic techniques contain a void in providing a means for measuring temperature and concentration in a plane/volume with instantaneity and simultaneity.

In this paper, a similar tomographic technique is described in which holography is used to accomplish the difficult task of simultaneously recording multiple-wavefront characteristics (i.e., phase and amplitude). The technique is amenable to reactive flow systems, affords excellent temporal and spatial resolution, and can be directly extended to provide three-dimensional resolution. The technique determines temperature and species concentration simultaneously through the use of interferometry and absorption with holography.

Background

For many years gas density in a flowing system has been determined optically using conventional interferometry. In this technique, the probe wave is passed through the object field and mixed with a path-matched reference wave. The resulting interference fringes, recorded on photographic film, depict the pathlength integral of the phase shift subjected to the probe wave. In a gaseous medium, the phase velocity v_p is dependent on the mass density ρ.[12] The mathematical representation is expressed in terms of refractive index, $n = c/v_p$, where c is the vacuum speed of light,

$$n - 1 = K\rho \tag{1}$$

where K is the Gladstone-Dale constant and is very weakly wavelength-dependent for most gases. The instrument that provides such measurements is the Mach-Zehnder interferometer.

Recent advances in holography, as used in conjunction with interferometry, have made simplifications in this interferometric technique.[13,14] Two key improvements of holo-

Presented as Paper 84-0202 at the AIAA 22nd Aerospace Sciences Meeting, Reno, NV, Jan. 9-12, 1984; received Sept. 19, 1984; revision submitted June 3, 1985.

*Research Scientist. Member AIAA.
†Research Scientist.
‡Research Scientist, General Productions Division.

graphic interferometry are:

1) The geometrical relation between the probe wave and the reference wave (i.e., the fringe spacing and orientation) can be adjusted after the experiment because these waves are recorded on separate plates.

2) The optical system phase errors, sometimes unavoidable in conventional interferometry, are canceled because the probe and reference beams traverse the same optical path.

A sample holographic interferogram obtained from the reconstruction of two holographic plates (one is for reference and the other is with the flow) is presented in Fig. 1. The interferogram depicts a striking visualization of the large-scale eddy observed in an argon-air flow interface observed in the California Institute of Technology two-dimensional mixing-layer facility. For two-component isothermal flows, the refractivity changes are interpreted in terms of species concentration or mass fraction changes. In a situation where temperature-related density changes occur, the additional change in the refractive index due to density cannot be distinguished. Hence, in multiple-component flows experiencing exothermic reactions, conventional interferometry is incapable of providing concentration measurements, not to mention temperature information; thus, an additional measurement is required.

Resonant Interferometry

Recent studies by Bershader et al.[15,17] and Blenstrup et al.[16] have identified the potentiality of interferometry when the wavelength is selected near the resonant state of a gas component. Near resonance, the refractive index becomes very dependent on wavelength—the factor $(n-1)$ increases a thousandfold or more. Also near resonance, the internal state of the gas species is being excited by absorption. The absorption of the gas species varies from negligible at off resonance to a large value at resonance. For atomic species, Bershader's analysis provides the dispersion relations for the refractive index and absorption coefficient as functions of temperature and number density. The spectral distribution near resonance for the refractive index and absorption coefficient in the vicinity of a resonant line are depicted in Fig. 2. The absorption coefficient has the typical absorption Voigt profile caused by Doppler and collision broadening. The refraction index, however, when expressed as $(n-1)$, appears as an odd function of frequency, increasing with frequency toward resonance, then decreasing as it passes through resonance, and eventually rising asymptotically to the off-resonant value. This peculiar behavior in refractive index is typical near resonance of any medium. As a result, the value of K increases near resonance. For the sodium D-line, Bershader et al.[15] and Blenstrup et al.[16] have shown it to be 1000 times or more and will provide the same amount of improvement in sensitivity.

The dispersion relations for n and κ have an interesting inference. Each has two independent variables in temperature T and species concentration N coupled together. In resonant interferometry where refractivity is considered, only one of the two variables can be determined—normally the concentration. If temperature is related to density by a gas law or is known, the closure exists. Because of the resonance behavior, the resonant interferometric technique has a potential application in quantifying the concentration of individual components in a gas mixture. If the spectral behavior of both the refractive index and the absorption coefficient is known, the dispersion relations provide the means to uncouple temperature and concentration. Resonant holography is used as the measurement technique for the determination of *both* refractive index and absorptivity.

Resonant Holography

Holography recording of a coherent optical wave, which has suffered resonant interaction with the species to be detected, stores the amplitude and phase of the wavefront with extremely high temporal and spatial resolution (temporal resolution $\simeq$ laser pulse width, $t \simeq 10$ ns; spatial resolution $\simeq 10$ μm). In resonant holography, two holograms are obtained, as in conventional holographic interferometry, corresponding to the cases of "with the flowfield" (probe wavefront) and "without the flowfield" (reference wavefront). Two reconstructions are required to obtain the refractivity and absorptivity data. In the former respect, the procedure follows holographic interferometry such that the wavefronts recorded in the presence and absence of the resonant species are superimposed resulting in interference fringes, which identify or code the optical phase shift. In the latter respect, the probe wavefront is reconstructed and the two-dimensional intensity distribution is acquired. The reference wavefront is similarly reconstructed for a second intensity distribution. The ratio of the two intensities provides the path-integrated absorption.

The resonant holography described previously provides the path-integrated refractivity and absorptivity and is applicable for a one-dimensional (1-D) system where the pathlength is known. For the axisymmetric case, Abel inversion techniques can be applied to spatially resolve the refractivity and absorptivity.[17,18,19] For the two-dimensional (2-D) case, one recognizes that the technique lends itself naturally to optical tomography. To produce the information for tomographic reduction, several "views" of the object field, obtained simultaneously, are required.[20,21] The extension of the technique to three-dimensional (3-D) application becomes obvious after the generalization to the 2-D case. The data obtained at each slice of the object field will be treated separately as in the 2-D case. This is repeated for each slice until the entire 3-D construction is complete. The extension

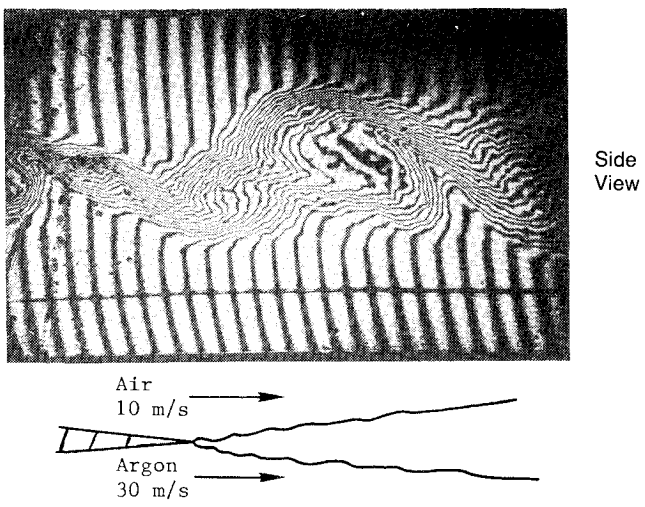

Fig. 1 Side view of 2-D mixing layer in California Institute of Technology facility.

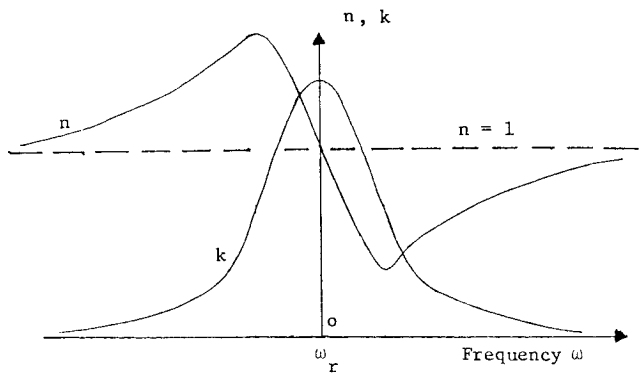

Fig. 2 Refractive index and absorption profiles near resonance.

of resonant holography to the 2- and 3-D cases is the ultimate potential of the technique.

Theoretical Analysis

Resonant holographic absorption and refraction tomography (RHART) involves the selective excitation of one of the absorption lines of the species of interest and holographic recording of the phase shift and amplitude attenuation of the transmitted laser beam. The integrated absorption along the line of sight is measured in the image plane of the reconstructed hologram, while the phase shift proportional to the integrated refraction can be measured by holographic interferometry. Since the absorption coefficient α and phase shift ϕ are functions of the number density N and translational temperature T of the molecule of interest, the measurements provide a set of two equations in two unknowns, such that

$$\alpha=\alpha(T, N) \tag{2}$$

$$\phi=\phi(T, N) \tag{3}$$

A semiclassical model of linear dispersion has been used to derive the functional relationship of Eqs. (2) and (3). A convolution process is modeled to convert the measured quantities, α and ϕ, into the physical parameters, T and N, such that

$$T=T(\alpha,\phi) \tag{4}$$

$$N=N(\alpha,\phi) \tag{5}$$

In the following, the concept of linear dispersion is outlined followed by a derivation of Eqs. (2) and (3). The motivations of choosing the hydroxyl radical to be the candidate species and its spectroscopic characteristics are then discussed.

Concept of Linear Dispersion

The linear theory of light dispersion implies that the electric polarization induced in the medium due to an incident electric field is linearly proportional to the amplitude of that field. The proportionality constant, called susceptibility, describes the phase deviation and amplitude attenuation of the incident field through the real and imaginary parts of the susceptibility, respectively.

The constitutive relation for linear dispersion can be described as

$$P(r,\nu)=\chi(\nu)E(r,\nu) \tag{6}$$

where P is the electric dipole moment per unit volume (electric polarization vector), E the electric field vector, and χ the susceptibility tensor which is a function of frequency, ν.

Since the susceptibility is analytic in the upper half-plane of the frequency domain, Cauchy's theorem can be used to relate the real and imaginary parts of $\chi(\nu)$ on the real axis. These relations are called Kramers-Kronig relations and are given as

$$n(\nu)-1=\frac{1}{\pi}\mathrm{PV}\int_{\infty}^{\infty}\frac{\kappa(\nu')}{\nu'-\nu}d\nu' \tag{7}$$

$$\kappa(\nu)=\frac{1}{\pi}\mathrm{PV}\int_{\infty}^{\infty}\frac{n(\nu')-1}{\nu'-\nu}d\nu' \tag{8}$$

where the refractive index n and the absorptivity κ constitute the real and imaginary parts of the susceptibility, respectively, and PV denotes Cauchy's principal value.

Kramers-Kronig relations indicate the dependence of the refractivity at a given frequency on the spectral profile of the absorption line and vice versa. However, the knowledge of the absorptivity at one frequency does not allow calculation of the refractivity using the K-K relations, unless another parameter is known; namely, temperature or number density. Therefore, measurement of n and κ at a given frequency does not violate the physical constraint imposed by the Kramers-Kronig relations but rather provides two independent measurements that can be convoluted into temperature and number density. Classical absorption measurements require the knowledge of the spectral profile of the absorption line which is described by two parameters: strength and width. Those two parameters are then used to determine T and N. In the present case, measuring n and κ is equivalent to measuring the spectral profile of one of the absorption lines with far more sensitivity, particularly for temperature measurements.

Both homogeneous and inhomogeneous line-broadening mechanisms contribute to the spectral profiles of absorptivity and refractivity. Homogeneous line broadening, $\Delta\nu$, which includes natural and collision broadening, is modified by Doppler or inhomogeneous broadening, $\Delta\nu_D$, to yield the

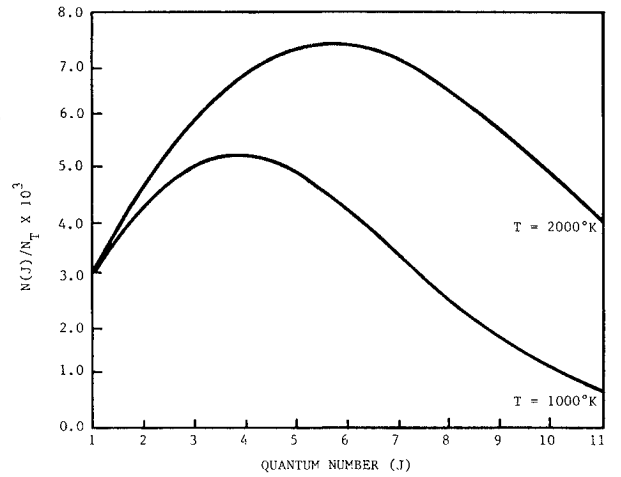

Fig. 3 Boltzmann's OH population distribution for different rotational levels.

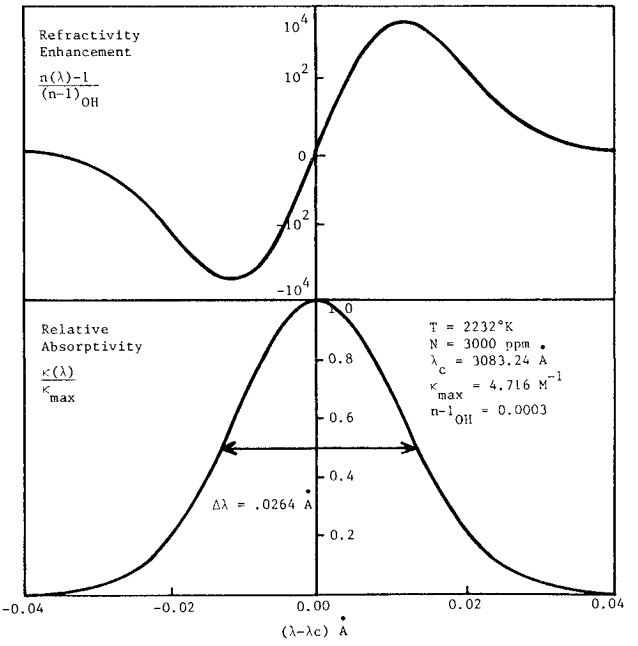

Fig. 4 Dispersion profile of OH near the $Q_1(4)$ resonance line.

Voigt line shape, defined as

$$V_1(a,\xi)=\frac{a}{\pi}\int_{\infty}^{\infty}\frac{(\xi-y)e^{-y^2}}{(\xi-y)^2+a^2}dy \tag{9a}$$

$$V_2(a,\xi)=\frac{a}{\pi}\int_{\infty}^{\infty}\frac{e^{-y^2}}{(\xi-y)^2+a^2}dy \tag{9b}$$

where

$$a=\frac{\Delta\nu}{\Delta\nu_D}\sqrt{\ell n 2} \tag{10a}$$

$$\xi=(\nu-\nu_{J'J''})\frac{2\sqrt{\ell n 2}}{\Delta\nu_D} \tag{10b}$$

$$y=(\nu'-\nu_{J'J''})\frac{2\sqrt{\ell n 2}}{\Delta\nu_D} \tag{10c}$$

where $\nu_{J'J''}$ is the resonance frequency of the transition $J''\rightarrow J'$. The functions $V_1(a,\xi)$ and $V_2(a,\xi)$ are the line profiles for refraction and absorption, respectively.

The spectral profiles of refractivity and the absorption coefficient, as derived from the linear theory of dispersion, are

$$n(\nu)-1=N_{J''}f_{J'J''}(C_1/\Delta\nu)V_1(a,\xi) \tag{11a}$$

$$\kappa(\nu)=N_{J''}f_{J'J''}(C_2/\Delta\nu_D)V_2(a,\xi) \tag{11b}$$

where $N_{J''}$ is the number density at level J', $f_{J'J''}$ the oscillator strength of transition $J''\rightarrow J'$; and C_1 and C_2 are constants that depend on molecular characteristics of the species of interest. Equations (11) show the linear dependence of n and κ on the number density, while the temperature dependence is included in the Voigt parameters a and ξ and the line widths $\Delta\nu$ and $\Delta\nu_D$.

At thermodynamic equilibrium the population of level J'' is related to the total number density by Boltzmann's distribution such that

$$\frac{N_{J''}}{N_1}=g_{J''}\frac{\exp(-E_{J''}/kT)}{Q} \tag{12}$$

where N_1 is the total population of the ground electronic state, $g_{J''}$ and $E_{J''}$ the degeneracy and energy of level J'', k Boltzmann's constant, and Q the partition function.

Species Selection

The hydroxyl molecule has been chosen for the experiment because 1) it appears naturally in all hydrocarbon-air reactions,[22-25] 2) it is the key molecule for product formation,[26,27] and 3) the spectroscopic characteristics of OH have been extensively studied and are available in the literature.[28-30]

Spectroscopically OH can be modeled as a two-level molecule, where transitions occur between the ground electronic $X^2\pi$ state and the excited $A^2\Sigma^+$ state. However, there are predissociative states $^4\Sigma^-$, $^2\Sigma^-$, and $^4\pi$ that cross the $A^2\Sigma^+$ potential. The $^4\Sigma^-$ state crosses the $^2\Sigma^+$ state at a fairly low vibrational level and must be avoided. For practical applications $X^2\pi$ and the combined $A^2\Sigma^+$ electronic states are the most significant. At equilibrium the populations of various states are determined by the Boltzmann distribution.

The population distributions at the different rotational quantum numbers for $x^2\pi$ have been calculated for different temperatures and are shown in Fig. 3. It is important to notice that the maximum population in the temperature range of interest occurs at relatively high rotational quantum numbers. Since the strength of the absorption line and number of fringes is increased (hence, increasing the sensitivity) by optimizing the quantity $N_{J''}f_{J'J''}$ [see Eqs. (11)], the excitation frequency should be selected to maximize the signal.

The line oscillator strength $f_{J'J''}$ of OH may be expressed in terms of the pure rotational band transition probability $S_{J'J''}$[31]:

$$f_{J'J''}=f_{v'v''}S_{J'J''}T_{J'J''}/4(2J''+1) \tag{13}$$

where $f_{v'v''}$ is the rotationless molecule band oscillator strength and $T_{J'J''}$ the vibration-rotation interaction correction factor. Superscripts (′) and (″) have their usual meaning indicating vibrational or rotational states at the upper and lower electronic levels, respectively. The rotational transition probabilities $S_{J'J''}$ for OH have been calculated by Dieke and Crosswhite[28] and are normalized as follows:

$$\sum_{J'}S_{J'J''}=4(2J''+1) \tag{14}$$

The rotationless molecule band oscillator strength $f_{v'v''}$, which is considered constant over a given vibration-rotation band, has been calculated by Rouse and Engleman[32] for the O-O band.

The absorption line has been selected to be an isolated line corresponding to one of the main transitions of

$$\mathrm{OH}(X^2\pi,v'',J'',K'')\underrightarrow{h\nu}\mathrm{OH}(A^2\Sigma^+,v',J',K') \tag{15}$$

The absorption line should also satisfy the criterion of maximizing $N_{J''}f_{J'J''}$ in order to optimize the sensitivity. Therefore, the $Q_1(4)$ transition has been chosen for this study.

Dispersion profiles of OH in CH_4-air flames are shown in Fig. 4 where the spectral behavior of the absorptivity and refractivity is shown near the $Q_1(4)$ line. The absorption curve, which is symmetric around the resonant frequency, is normalized by the maximum value of absorption at resonance. The refractivity curve, which is asymmetric, has been normalized on the value of OH of nonresonance refractivity under standard pressure and temperature.

Experimental Considerations

Resonant holography takes advantage of the most powerful feature of holography, that both the amplitude and phase of coherent optical waves are recorded. This two-variable measurement technique makes holography particularly attractive for spectroscopic diagnostics of gases where both temperature and concentrations are unknown. The theoretical development of the dispersion relations shows that the refraction and absorption at a fixed wavelength are independent quantities and, therefore, can be used to determine the dependent variables—temperature and concentration.

Absorption Measurements

The line-of-sight integrated absorption is measured in the image plane of the reconstructed hologram. The ratio of detected intensity from the signal hologram (recorded near the resonance frequency) to the reference hologram (recorded far from the resonance frequency) yields the level of absorption, α.

Beer's law gives the relation between incident and transmitted beams,

$$I_\nu(L)=I_\nu(0)\exp\left(-\int_0^L\kappa_\nu(x)dx\right) \tag{16}$$

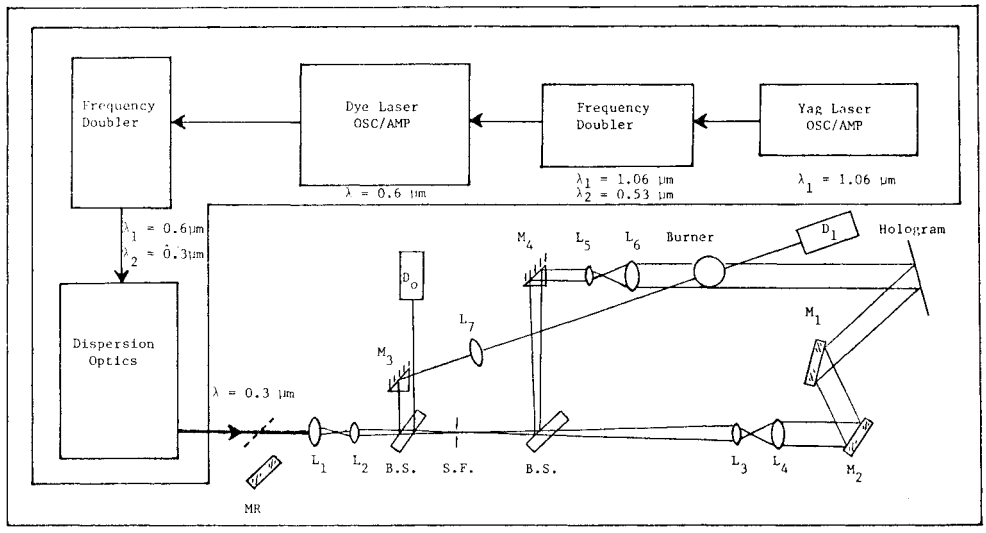

L_1 : f = 200 mm, ϕ = 50 mm
$L_{2,3,5}$: f = 100 mm, ϕ = 25 mm
$L_{4,6,7}$: f = 500 mm, ϕ = 50 mm
$D_{o,1}$: Absorption Photodetectors
$M_{1,2}$: Dielectric Coated Mirrors
$M_{3,4}$: Corner Cubes
B.S. : Beam Splitter
MR : Reconstruction Mirror

Fig. 5 Resonant holography optics schematic (Sandia Combustion Research Facility).

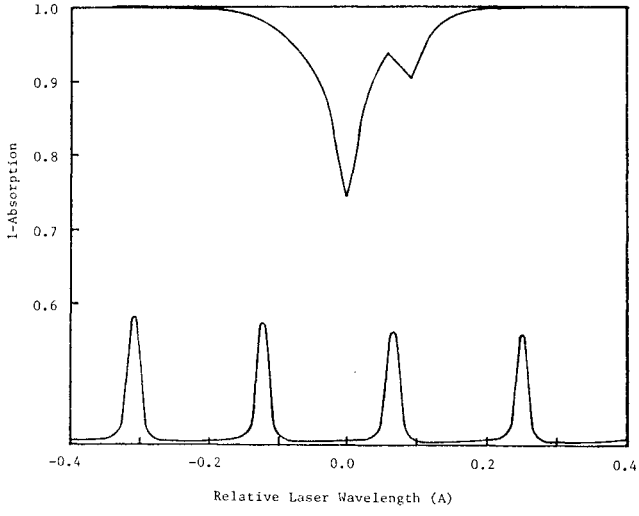

Fig. 6 Measured absorption spectrum for the $Q_1(4)$ transition of OH; also plotted is output from Fabry-Perot interferometer of dye laser beam (λ = 6166 Å).

where L is the optical pathlength. The detected signal is the integral of Eq. (18) over the laser bandwidth

$$I(L) = I(0)\int_{\Delta\nu_L} g(\nu)\exp\left(-\int_0^L \kappa_\nu(x)\mathrm{d}x\right)\mathrm{d}\nu \tag{17}$$

where the laser line shape $g(\nu)$ and the laser line width $\Delta\nu_L$ are introduced. Therefore, the transmissivity, $\alpha = I(L)/I(0)$, is related nonlinearly to the absorption coefficient κ_ν, as indicated by Eq. (17).

Refraction Measurements

The integrated refractivity of the gas mixture is determined by holographic interferometry. The phase ϕ is related to the refractivity such that

$$\phi - \phi_0 = \int_{\Delta\nu_L} g(\nu)\int_0^L (n(\nu) - n_0(\nu))\mathrm{d}x\mathrm{d}\nu \tag{18}$$

The phase shift is generally measured in terms of fringes or waves. The empirical Dale-Gladstone formula provides the relation between density or number density and refractivity, and for gas mixtures, the total refraction is the summation of constituents,

$$n_i - 1 = K_i N_i \tag{19}$$

where K_i is the Dale-Gladstone constant of the species. The K_i's are constant for any gas over a wide range of pressure with a weak dependence on wavelength in the visible portion of the spectrum.

Using the perfect gas law, $P = NkT$, Eq. (19) may be rewritten as

$$n(\lambda^0) - 1 = N(T)\sum_i K_i X_i \tag{20}$$

The bulk refractivity at resonant wavelengths is essentially unchanged except for the contribution from the resonant species

$$n(\lambda^*) - 1 = N(T)\sum_i K_i X_i + F(\lambda^*, T, N_{\mathrm{OH}}) \tag{21}$$

where the resonant refractivity, $F(\lambda^*, T, N_{\mathrm{OH}})$, is given by Eq. (11a) and λ^* is the wavelength for either of the refractivity extremum. Note that the OH refractivity, Fig. 5, has positive and negative extremum for wavelengths on the long and short wavelength sides of the absorption peak, respectively. Hence, for the long wavelength resonance the bulk refractivity is increased, and for the short wavelength resonance the bulk refractivity is decreased.

For nonresonant and resonant wavelengths, the phase shifts incurred between rays passing through and to the side of the flame are

$$\Delta\phi(\lambda^0) = \phi_a - \phi^0 = (n_a - 1)\frac{L}{\lambda^0} - (n_f(\lambda^0) - 1)\frac{L}{\lambda^0} \tag{22}$$

$$\Delta\phi(\lambda^*) = \phi_a - \phi^* = (n_a - 1)\frac{L}{\lambda^*} - (n_f(\lambda^*) - 1)\frac{L}{\lambda^*} \tag{23}$$

where the subscripts a and f denote ray paths through the air and flame, respectively, and the pathlength through the flame is denoted by L. The differential phase shift is

$$\Delta\phi^* = \Delta\phi(\lambda^*) - \Delta\phi(\lambda^0) \simeq (n_f(\lambda^*) - n_f(\lambda^0))\frac{L}{\lambda^*} + 0\left(\frac{\lambda^* - \lambda^0}{\lambda^*}\right) \tag{24}$$

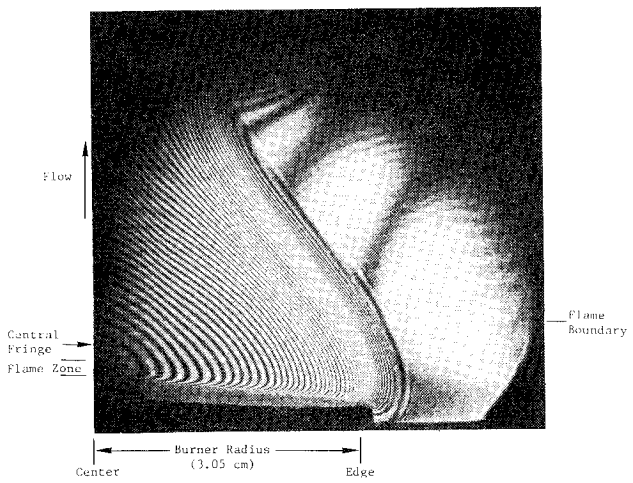

Fig. 7 Nonresonant interferogram.

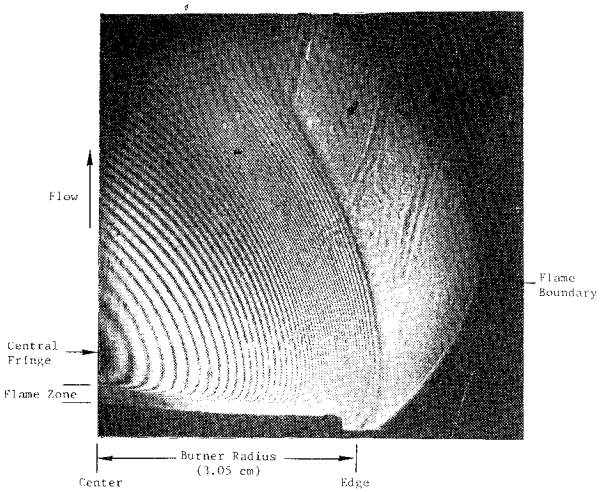

Fig. 8 Resonant interferogram.

The differential phase shift is directly proportional to the OH density and temperature.

$$\Delta\phi^* \simeq [n_f(\lambda^*) - n_f(\lambda^0)]\,(L/\lambda) \simeq F(\lambda^*, T, N) \qquad (25)$$

Experimental Apparatus

Burner

The experiment was performed on a flat flame burner, generically known as a "Pagni burner." The burner is constructed of sintered bronze which acts as a flame holder. The fuel-air mixture is thoroughly mixed in the plenum before passing through the flame holder. The premixed flame was stabilized at 1 mm above the burner rim by controlling the mass flow of both the fuel and air. The equivalence ratio of the experiment was 1.0. The burner is water-cooled, resulting in a relatively cool flame. The maximum flame temperature was measured to be 1600 ± 70 K using common interferometry.

Optical Arrangement

Figure 5 illustrates the experimental layout. A frequency-doubled Molectron YAG laser with an oscillator/amplifier has been used to pump a Quanta Ray frequency-doubled, pulsed-dye laser. The dye laser grating, etalon, and the frequency-doubling crystal alignments are computer-controlled to fine-tune the laser beam. The desired probe beam is obtained by separating the ultraviolet and visible outputs using dispersion optics. With the etalon installed in the dye laser, the output energy is 5 mJ with a relatively narrow line width of $\Delta\lambda = 0.22$ Å [full width at half maximum (FWHM)] at $\lambda = 3083.17$ Å.

The holographic requirements for OH resonance experiments dictated the use of fused silica transmission optics and holographic emulsions with sensitivity in the ultraviolet region of the spectrum. The optical system incorporates standard holographic elements such as spatial filter, beam splitter, reference and object beam expander/collimator, and holographic plate holder.[13] A line-of-sight absorption detector system was incorporated into the system to allow accurate positioning of the laser wavelength with respect to the OH absorption peak. A Kodak holography emulsion with sensitivity in the ultraviolet spectrum has been used.

Holographic Reconstruction and Measurements

Holographic reconstruction was accomplished with an argon-ion laser ($\lambda = 4880$ Å). The absorption measurement has been performed during the holographic recording process using line-of-sight detectors. Holographic interferometry has been done by exposing each plate in the presence and absence of the flame. The interferogram produced in reconstruction was photographed in the image plane of the burner. The hologram diffraction efficiency was generally excellent with bright images and high-contrast fringes. The temporal coherence of the frequency-doubled, pulse-dye laser was known to be excellent as indicated by the line width ($\Delta\lambda = 0.022$ Å). The uniformity of the reconstructed image indicated that the Quanta Ray system has both excellent spatial and temporal coherence. The holography construction optics were carefully designed to return equivalent parts of the object and reference beams to the same point on the hologram.

Experiment

The laser sytem utilizes precision computer-controlled scanning. The scanning capability allows absorption profiles to be recorded. Initially low-resolution absorption scans were used to locate the selected OH line, and finally high-resolution scans were used to obtain the absorption line profile. The laser wavelength was then adjusted to correspond to the wavelength where the absorption was one-half its resonance value.

Theoretical dispersion profiles (Fig. 4) showed a refractivity peak at such a position in the absorption profile. For nonresonant holograms the laser was tuned to a point in the spectrum with negligible absorption. For double-exposure resonant holograms, the wavelength was set and a hologram was recorded in the presence and absence of the flame.

The absorption profile of the $Q_1(4)$ line of the hydroxyl molecule is illustrated in Fig. 6. A Fabry-Perot etalon with 1 cm^{-1} free spectral range in the visible region has been used to monitor the excitation frequency scan across the absorption line. The strength of the absorption line at the resonant frequency (3083.24 Å) was 25% for the experimental conditions, with a burner diameter of 6.1 cm, and a laser line width of 0.022 Å FWHM. The weak absorption peak that appears to the right-hand side of the $Q_1(4)$ peak corresponds to the satellite transition $Q_{21}(4)$. The absorption line width (0.0612 Å) is wider than the predicted line width of 0.0264 Å (Fig. 5). This discrepancy may be attributed to the relatively wide laser line used to measure the absorption profile. Previous absorption measurements with a narrower laser line width, 2×10^{-4} Å, show that the absorption line width for the $Q_1(10)$ line was about 0.028 Å.[33]

Results

The nonresonant and resonant frequency interferograms are shown in Figs. 7 and 8, respectively. Note that the interferograms span only one side of the burner, and that a cen-

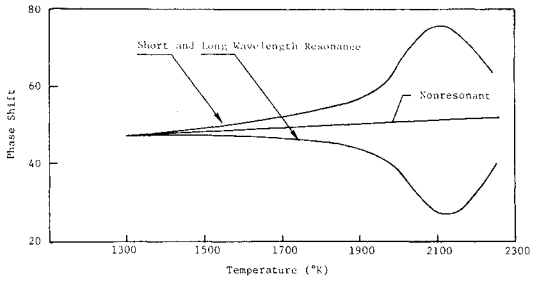

Fig. 9 Resonant and nonresonant phase shifts.

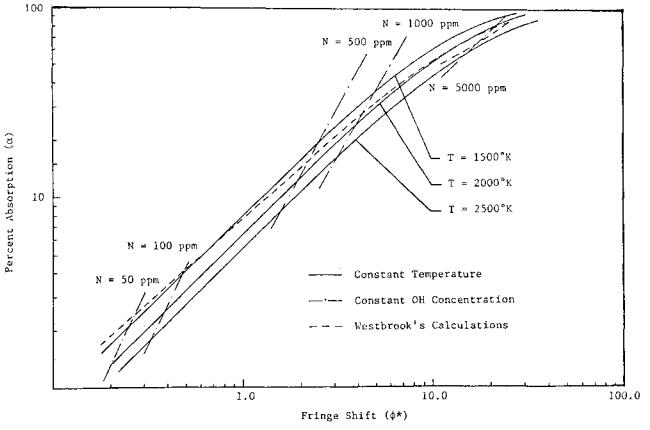

Fig. 10 Relationship between the dispersion parameters α, $\Delta\phi^*$, and OH temperature and concentration.

tral fringe is identified near the center of the burner. These interferograms were photographed in the focal plane of the burner to minimize beam steering effects, as suggested by Vest.[14] The fringe shift at the central fringe (i.e., the maximum) is 48 and 47 fringes for resonant and nonresonant frequencies, respectively (Fig. 9). The differential phase shift, Eqs. (24), is negative

$$\Delta\phi^* = \Delta\phi(\lambda^0) - \Delta\phi(\lambda^*) = -1 \text{ wave}$$

as was predicted by the theory equations (11) and (25) for the short wavelength resonance. Simplistic calculations based on the perfect gas law and equilibrium values of product concentrations show that a phase shift of a -1 fringe is in agreement with the measured phase shift from the experiment.

A map of the dispersion parameters (α, $\Delta\phi^*$) is calculated for different temperatures and number densities, Fig. 10. The map illustrates the relation between the measured quantities α and $\Delta\phi^*$ and the physical parameters T and N. The constant-number-density lines are straight lines, while the constant-temperature lines may be approximated as straight lines in the low-number density side and become exponential at the high-number-density side. The dotted line is Westbrook's kinetics calculations of T and the number density of OH molecules in CH_4-air flames which serves to bound the range of the physically acceptable values of T and N. The kinetics calculations have been used rather than their equilibrium counterparts to demonstrate the ability of the technique to respond to the superequilibrium values of the hydroxyl radical. The uniqueness of the resonance holography technique is observed over the range of the Westbrook calculation. The α-$\Delta\phi^*$ map shows that the method is more sensitive to number density fluctuations than temperature. Based on Westbrook's[34] calculations of CH_4-air flame kinetics, at 1600 K, OH concentration is 500 ppm. Figure 10 indicates that under those flame conditions the fringe shift based on OH should be one fringe, which is in agreement with the experiment.

Uncertainties in temperature and number density measurements, based on a refraction detectability limit of 0.1 fringe with 10% accuracy and absorption of 1% accuracy, show that the accuracy in N and T is 28 ppm and 55 K, respectively, at the adiabatic flame temperature of 2232 K and an equilibrium OH concentration of 3000 ppm at that temperature.

Conclusions

A theoretical validation of the resonant holography concept has been obtained and preliminary experiments have shown that holographic interferometry is a promising diagnostic technique even at OH resonance wavelengths in the ultraviolet spectrum. The linear dispersion theory has been applied to the hydroxyl radical resulting in a set of unique relations between the gas state (T and N) and the measured variables fringe shift and absorption.

CH_4-air flame has been considered. The mixture, including OH contribution, refractivity, and absorptivity, was computed for densities and temperatures in the range predicted by kinetics calculations for stoichiometric flames. The resulting variable map displayed a unique relation between the measured α and ϕ variables and the physical parameters T and N. The relations were developed using the laser line width achieved in the experiments, which was about one-third of the absorption line width.

Acknowledgments

This work was supported by the National Science Foundation under Grant DMR-82-60638; Mr. Richard Schoen, Project Officer. The authors would like to thank Dr. Mike Gusinow and Dr. John Goldsmith for their support of the collaborative experiments at the Sandia Combustion Research Facility.

References

[1]Crosley, D. R., ed., *Laser Probe for Combustion Chemistry,* American Chemical Society Symposium Series 134, 1980.

[2]Cattolica, R. J., "Laser Absorption Measurements of OH in a Methane-Air Flat Flame," Sandia National Laboratory, Energy Rept. No. SAND79-8717, 1979.

[3]Daily, J. W., "Laser-Induced Fluorescence Spectroscopy in Flames," *Laser Probe for Combustion Chemistry,* American Chemical Society Symposium Series 134, 1980, p. 61.

[4]Cattolica, R. J. and Stephenson, D. A., "The Temperature Field in a Hydrogen/Air Diffusion Flame from Two-Dimensional Laser Induced Fluorescence of OH," AIAA Paper 83-0404, 1983.

[5]Kychakoff, G., Howe, R. D., Hanson, R. K., and McDaniel, J. C., "Quantitative Visualization of Combustion Species in a Plane," *Applied Optics,* Vol. 21, No. 18, Sept. 1982, p. 3225.

[6]Robben, F., "Comparison of Density and Temperature Measurement Using Raman Scattering and Rayleigh Scattering," *Combustion Measurements: Modern Technique and Instrumentation,* edited by R. Goulard, Academic Press, NY, 1976.

[7]Lapp, M., "Raman-Scattering Measurements of Combustion Properties," *Laser Probe for Combustion Chemistry,* American Chemical Society Symposium Series 134, 1980, p. 207.

[8]Ekbreth, A. C., "Spatially Precise Laser Diagnostics for Practical Combustor Probing," *Laser Probe for Combustion Chemistry,* American Chemical Society Symposium Series 134, 1980, p. 271.

[9]Semerjian, H. G. and Santoro, R. J., "Laser Tomography for Diagnostics in Reacting Flows," AIAA Paper 82-0854, 1982.

[10]Ray, S. and Semerjian, H. G., "Laser Tomography for Simultaneous Concentration and Temperature Measurement in Reacting Flows," AIAA Paper 83-1553, June 1983.

[11]Santoro, R. J. et al., "Multiangular Absorption Measurements in a Methane Diffusion Jet," *Laser Probe for Combustion Chemistry,* American Chemical Society Symposium Series 134, 1980, p. 427.

[12]Ladenburg, R. and Bershader, D., "Interferometry" *Physical Measurements in Gas Dynamics and Combustion,* edited by R. Ladenburg, Princeton University Press, Princeton, NJ, 1954.

[13]Trolinger, J. D., "Laser Instrumentation for Flow Field Diagnostics," AGARDograph No. 186, 1974.

[14]Vest, C. M., *Holographic Interferometry,* John Wiley & Sons, New York, 1979.

[15]Bershader, D., Prakash, S. G., and Huhn, G., "Improved Flow Visualization by Use of Resonant Refractivity," *Progress in Astronautics and Aeronautics: Experimental Diagnostics in Gas Phase Combustion Systems,* edited by B. T. Zinn, Vol. 53, AIAA, New York, 1977, p. 595.

[16]Blenstrup, G., Bershader, D., and Langhoff, P., "Recent Results of Resonant Refracting Studies for Improved Flow Visualization," *Shock Tubes and Waves,* Proceedings of the 12th International Symposium on Shock Tubes and Waves, The Magnes Press, Jerusalem, 1980.

[17]Bershader, D., "Some Aspects of the Refractive Behavior of Gases," *Modern Optical Methods in Gas Dynamics Research,* edited by D. Dosanjh, Plenum Press, New York, 1977, pp. 65-83.

[18]Chen, F. P. and Goulard, R., "Retrieval of Arbitrary Concentration and Temperature Fields by Multiangular Scanning Techniques," *Journal of Quantitative Spectroscopy and Radiative Transfer,* Vol. 16, 1976, p. 819.

[19]Blair, D. W., "An Analysis of Error Propagation in Abel Inversions of Spectral Emission Absorption Data," *Journal of Quantitative Spectroscopy and Radiative Transfer,* Vol. 14, 1974, p. 325.

[20]Santoro, R. J., Semerjian, H. G., Emmerman, P. J., and Goulard, R., "Optical Tomography for Flow Field Diagnostics," *International Journal of Heat and Mass Transfer,* Vol. 24, 1981, p. 1139.

[21]Semerjian, H. G., Santoro, R. J., Goulard, R., and Emmerman, P. J., *Fluid Mechanics of Combustion Systems,* edited by T. Morel, R. P. Lohman, and J. Rackley, ASME, New York, 1981, p. 119.

[22]Tsatsaronis, G., "Prediction of Propagating Laminar Flames in Methane, Oxygen, Nitrogen Mixtures," *Combustion and Flame,* Vol. 33, 1978, p. 217.

[23]Smoot, D. L., Hecker, W. C., and Williams, G. A., "Prediction of Propagating Methane-Air Flames," *Combustion and Flame,* Vol. 26, 1976, p. 323.

[24]Semenov, M. N., *Some Problems in Chemical Kinetics and Reactivity,* translation by M. Boudart, Vol. 1, 1958; Vol. 2, 1959, Princeton University Press, Princeton, NJ.

[25]Guirguis, R. H., Oppenheim, A. K., Karasola, I., and Creighton, J. R., "Thermochemistry of Methane Ignition," presented at the Seventh ICOGER, Gottingen, FRG, Aug. 1979, p. 134.

[26]Creighton, J. R., "A Two Reaction Model of Methane Combustion for Rapid Numerical Calculations," Lawrence Livermore Laboratory, Livermore, CA, Preprint UCRL-79669, Rev. 1, 1979, pp. 1-21.

[27]Azzazy, M. and Daily, J. W., "Fluorescence Measurements of OH in a Turbulent Flame," *AIAA Journal,* Vol. 21, Aug. 1983, p. 1100.

[28]Dieke, G. H. and Crosswhite, H. M., "The Ultraviolet Bands of OH; Fundamental Data," *Journal of Quantitative Spectroscopy and Radiative Transfer,* Vol. 2, 1962, p. 97.

[29]Bass, A. M. and Broida, H. P., "A Spectrophotometric Atlas of the $^2\Sigma^+ - {}^2\pi$ Transition of OH," National Bureau of Standards, Washington, DC, NBS Circular 541, June 26, 1953.

[30]Chidsey, I. L. and Crosley, D. R., "Calculated Rotational Transition Probabilities for the *A-X* System of OH," *Journal of Quantitative Spectroscopy and Radiative Transfer,* Vol. 23, 1980, p. 187.

[31]Anketell, J. and Perry-Thorne, A., "Oscillator Strengths in the $^2\Sigma^+ - {}^2\pi$ Band System of OH by the Hook Method," *Proceedings of the Royal Society of London,* Vol. A301, 1967, p. 343.

[32]Rouse, P. E and Engleman, R., "Oscillator Strengths From Line Absorption in a High-Temperature Furnace—I. The (0,0) and (1,0) Bands of the $A^2\Sigma^+ - X^2\pi$ Transition in OH and OD," *Journal of Quantitative Spectroscopy and Radiative Transfer,* Vol. 13, 1973, p. 1503.

[33]Lück, K. C. and Thielen, W., "Measurements of Temperature and OH Concentrations in a Lean Methane-Air Flame Using High Resolution Laser Absorption Spectoscopy," *Journal of Quantitative Spectroscopy and Radiative Transfer,* Vol. 20, 1979, p. 71.

[34]Westbrook, C. K., "An Analytical Study of Shock Tube Ignition of Mixtures of Methane and Ethane," *Combustion Science and Technology,* Vol. 20, 1980, p. 5.